Nuclear Instruments and Methods in Physics Research A 863 (2017) 62–73

Contents lists available at ScienceDirect

Nuclear Instruments and Methods in Physics Research A

journal homepage: www.elsevier.com/locate/nima

Neutron – Alpha irradiation response of superheated emulsion detectors

M. Felizardo [a,*], T. Morlat [a], T.A. Girard [a,b], A. Kling [a], A.C. Fernandes [a], J.G. Marques [a], F. Carvalho [a], A.R. Ramos [a], (SIMPLE Collaboration)

[a] Centro de Ciências e Tecnologias Nucleares, Instituto Superior Técnico, Universidade de Lisboa, E.N. 10, 2695-066 Bobadela, Portugal
[b] Departamento de Física, Universidade de Lisboa, 1749-016 Lisboa, Portugal

ARTICLE INFO

Article history:
Received 5 January 2017
Received in revised form
4 May 2017
Accepted 7 May 2017
Available online 10 May 2017

Keywords:
Neutron and alpha irradiation response;
Superheated emulsion detectors

ABSTRACT

We report new experimental investigations of the response of single superheated emulsion detectors with small droplet (< 30 μm radii) size distributions to both α- and neutron irradiations. Analysis of the results in terms of the underlying detector physics yields a toy model which reasonably reproduces the observations, and identifies the initial energy of the α in the liquid and distribution of droplet sizes as primarily responsible for the detector capacity to distinguish between nuclear recoil and α events.

1. Introduction

The impact of any particle detector is often dependent on its ability to discriminate between detector-recorded, particle-induced backgrounds. Among the various detector types in present use are superheated liquid devices. These generally consist of either superheated emulsion detectors (SEDs): comprising distributions of micrometric liquid droplets in a gel-like medium (SDDs) or rigid polymer matrix (BDs) [1], or bulk liquid bubble chambers. Both record the acoustic signal associated with the particle-induced bubble nucleation event, as well as other non-particle acoustic backgrounds associated with environmental noise. Due to the thermodynamics of the detector response, particle sensitivity in moderately superheated devices is essentially reduced to high linear energy transfer (LET) radiations; an intrinsic low LET particle insensitivity of better than 10^{-10} has been demonstrated by γ and electron irradiations [2]. With increasing liquid superheat, this insensitivity decreases and the devices record these events also.

SEDs have been investigated for a number of radiation detection applications including nuclear, health, medical, and space physics [1,3] involving neutron, proton, heavy ion, electron and γ-ray fields. Because of their application to the direct search for astroparticle dark matter, which is critically dependent upon their ability to isolate low energy nuclear recoil events (< 100 keV) generated by elastic scattering of weakly interacting massive particles from naturally-occurring, low level neutron and α backgrounds in the materials, the question of particle response in superheated liquid devices has come under severe scrutiny and a large part of the advances in their capabilities has emerged from two experiments. In 2008, the PICASSO project using C_4F_{10} dispersed in a Gaussian droplet distribution with mean of $<r_d> = 100 \pm 25$ μm, high frequency piezo instrumentation, and irradiations effected with AmBe (neutron) and ^{241}Am and/or ^{226}Ra doping (α), reported a partial separation of the neutron-generated recoil-α acoustic event amplitude (A) distributions [4]. In 2010, the SIMPLE project independently reported [5] a full separation of the two power distributions in irradiations of separate devices, using C_2ClF_5 with a Gaussian droplet distribution of $<r_d> = 30 \pm 7.5$ μm, a low frequency electret microphone, U_3O_8 α-doping and neutron irradiations with either AmBe or epithermal neutrons from the Portuguese Research Reactor (PRR) [6], which was attributed to the difference in proto-bubble formation. In 2011, PICASSO presented "new insights" into the detector response, this time with the same SEDs but based on the recorded event acoustic energy [7] obtained by squaring the waveform of each transducer signal and integrating over its duration, which also identified the difference in recoil-α proto-bubble formation as the determining factor for the separation of the two response distributions. Experimentally, however, only a partial separation between the recoil-α events was again obtained, and only in the case of ^{226}Ra α-calibrations. The difference between the results of the two projects has since remained unresolved [8].

* Corresponding author.

http://dx.doi.org/10.1016/j.nima.2017.05.008
0168-9002/

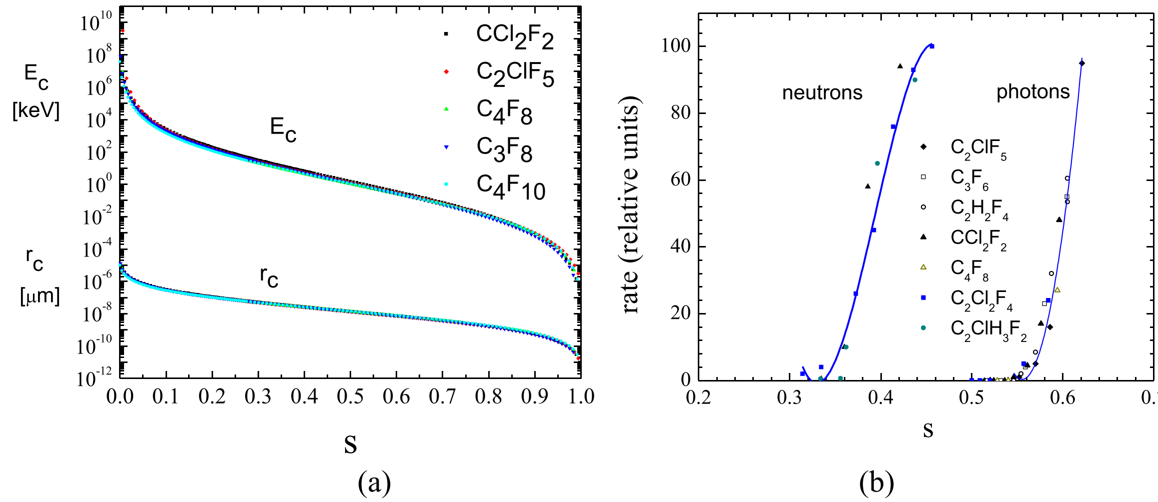

Fig. 1. (a) Universal behavior of E_c and r_c in terms of s; (b) γ and neutron irradiation responses of various superheated liquids, which in s fall on single curves (adapted from Ref. [21]).

Other researchers have since contributed to the issue of particle response, principally however with respect to neutron-generated nuclear recoil and γ events [9,10]. Das et al. recently reported [11] recoil-α response studies using CCl_2F_2, a low frequency condenser microphone, a bimodal Gaussian distribution of small droplet sizes (58% $<r1>\sim 3\pm1$ μm, 42% $<r2>\sim 25\pm5$ μm), and irradiations with neutron (AmBe) and a solid α source (^{241}Am) – the latter which, in contrast to the usual emitter-doping, was positioned outside the SED gel. Analysis of the data via the acoustic signal energy demonstrated an inversion of the recoil - α response amplitudes, accompanied by a significant overlap of the two distributions.

The detectors of each experiment differ in various aspects: superheated liquid and concentration, droplet sizes, gel composition and stiffness, size and volume of detectors, operating temperatures and pressures, instrumentation, signal acquisition and analysis. We here examine the response issue in small ($r_d < 30$ μm) droplet size distribution SEDs, towards providing an improved understanding of the involved mechanics for general use in future SED implementations. Section 2 summarizes the bubble nucleation physics underlying SED performance. Section 3 describes new experiments using single SEDs with several droplet size distributions and modified gel stiffness, and discusses the results. Section 4 elaborates on the particle-superheated liquid interactions, and introduces a simple model of the SED response which is seen to reproduce well the experimental results. The difference in number of proto-bubbles created by recoil target ion and α's, the initial energy of the α in the liquid, and the differences in droplet size distributions, are identified as the basis for the particle response. A summary of conclusions is given in Section 5.

2. Irradiation response

The general physics of detector operation, based on the "thermal spike" model of Seitz [12], has been described by various authors [13–21] (and references therein). The process consists of several stages beginning with the incident particle energy deposition in a small ($\sim 3\times10^{-4}$ μm^3) volume of the liquid, creating ionization electrons which generate a localized, high temperature region (the "thermal spike"). The resulting sudden vaporization of the region and its expansion generates a shock wave in the droplet, in which the temperature and pressure within the shock enclosure initially exceed the critical temperature and pressure of the liquid: there is no distinction between liquid and vapor, and no bubble. As the energy is transmitted from the thermalized region to the surrounding medium through shock propagation and heat conduction, the temperature and pressure of the fluid within the shock enclosure decrease and the expansion process slows [17]. As the temperature and pressure continue decreasing to their critical values, a vapor-liquid interface is formed which may generate a proto-bubble of submicron critical radius $r_c = 2\sigma(T)/\Delta p$ of the vapor state at which the pressure difference ($\Delta p = p_v - p_l$, with v=vapor, l=liquid) overcomes its surface tension σ. If this is not achieved, growth is impeded by interface/viscous forces and conduction heat loss, and the proto-bubble collapses; otherwise, the droplet evaporation generates an expanding gas bubble, accompanied by a pressure wave. The time scale for proto-bubble creation is sub-nanosecond; complete droplet evaporation occurs over milliseconds.

Only 2–6% of the total energy release appears acoustically. The acoustic energy release is given by [22]:

$$E = A^2\tau = -\frac{4\pi\rho_l}{3c}\frac{r_b^6}{\tau^3}, \tag{1}$$

from which the acoustic power is

$$K = A^2 = \frac{4\pi\rho_l}{c}\frac{r_b^6}{\tau^4}, \tag{2}$$

where ρ_l is the liquid density, c is the speed of sound in the liquid, $r_b=r_b(\tau)$ is the bubble radius, τ is the expansion time of the bubble, and A is the signal amplitude.

Proto-bubble formation occurs if the particle energy deposition (E) satisfies [12]:

$$E \geq E_c = 4\pi r_c^2\left(\sigma - T\frac{\partial\sigma}{\partial T}\right) + \frac{4\pi}{3}r_c^3\rho_v h_v - \frac{4\pi}{3}r_c^3\Delta p \tag{3}$$

and

$$dE/dx \geq E_c/L_c \equiv LET_c, \tag{4}$$

where T is the SED operating temperature, $\rho_v(T)$ is the vapor density, and $h_v(T)$ is the heat of vaporization. The E_c/L_c is the critical deposited energy density required for proto-bubble nucleation, with $L_c = \Lambda r_c$ the effective ionic energy deposition length, and Λ an empirical liquid-dependent parameter. Both E_c and r_c, when displayed as a function of the reduced superheat $s=(T-T_b)/(T_c-T_b)$ with T_c, T_b the critical and boiling temperature of the liquid at a given pressure [21] respectively, are seen to provide "universal" curves for different liquids (Fig. 1(a)). Similarly, the response of the SEDs to a given irradiation type lie on "universal" curves when displayed in s (Fig. 1(b)); sensitivity to γ's and electrons is seen for $s \geq 0.51$, increasing with s.

Unlike E_c and r_c, Λ however appears to exhibit no universal behavior when evaluated in terms of reduced superheat [23]. Whereas r_c and E_c are well-defined thermodynamically, Λ is without concrete theoretical basis and must be determined experimentally. It is constant for a liquid at a given T, p_l [24]. It generally ranges from 2 to 12.96 [21], with reported values increasing up to 20 and larger for neutron-induced recoil thresholds above 1 MeV [24–28]. Studies with heavy ions indicate that Λ may also depend on the ion mass number, decreasing with number increase [29].

3. New irradiation results and discussion

All measurements were performed using 150 ml versions of the standard ($<r> = 30 \pm 7.5$ μm) SIMPLE science (900 ml) detector. Because of uncertainties in the recompression capability to restore the original droplet size distribution, several pairs of near-identical SEDs were fabricated, one of which was neutron-then-α irradiated, and the second with the sequence reversed. The following pairs of SEDs were considered:

(i) two C_2ClF_5 SEDs (1.3% and 1.4%wt) fabricated to provide a droplet size distribution peaked at $\sim 10 \pm 1$ μm.
(ii) two C_2ClF_5 SEDs (1.3% and 1.8%wt) similarly fabricated, with a reduced liquid fractionating time to yield a droplet size distribution peaked at $\sim 23 \pm 3$ μm.
(iii) a third pair of SEDs (1.3% and 2.1%wt) made with a stiffer gel by adding twice as much gelatin. The liquid fractionating time was adjusted to provide a droplet size distribution peaked at $\sim 10 \pm 1$ μm.

Two additional SEDs were also fabricated:

(iv) a 150 ml SED with the stiffer gel (as above) and 2.3 g (1.3%wt) of C_4F_{10} fractionated to give a larger distribution peaked at $\sim 23 \pm 3$ μm.
(v) a 150 ml SED with the standard gel and 3 g (1.7%wt) of C_2ClF_5 fractionated to give a droplet distribution peaked at $\sim 5.5 \pm 3$ μm.

From polarimetry measurements, the rate of helix formation $\chi = 0.50$ [30]: since the helix concentration is $c_{helix} = \chi c_{gel}$ [31,32] and the standard gel $c_{helix} = 8 \times 10^{-3}$ g cm^{-3}, $c_{helix} = 16 \times 10^{-3}$ g cm^{-2} for the “stiff” SED. The elastic modulus is given by G' $= 325$ Pa leading to a Young's modulus of $Y_{standard} = 3$ G' $= 975$ Pa for the standard gel and $Y_{stiff} = 6$ kPa [30]. In the case of PICASSO, with a concentration of acrylamide ~ 6% and Bis-acrylamide $= 0.16\%$, $Y_{PICASSO} = 5$ kPa according to [33], and the "stiff" gel reproduced that of PICASSO.

The droplet size distributions were measured in randomly-selected slices of each gel matrix, taken from randomly-selected sites in each SED volume, by an optical microscope (Olympus Model Bx 60 M). The results in each slice were similar. The resulting distributions were fit both with a Gaussian (mean $<R>$, σ) and a Lorentzian (peak $<R>$, Γ), and seen to exhibit the Lorentzian profile which included a non-negligible larger radii tail.

All SEDs but (v) were injected with 0.94 Bq of a U_3O_8 solution; the (v) SED was doped with 0.37 Bq of U_3O_8 during fabrication. Neutron irradiations were performed either on the γ-shielded PRR thermal column (Case (i) above) or with a 1 mCi AmBe source located at 1.5 m from the SEDs to provide 2–3 recoil events per min (Cases (ii)-(v)). Each SED was placed inside a temperature-controlled, circulating water bath; the bath temperature was thermometer- monitored with a 0.1 °C uncertainty. Detector responses were recorded for up to 24 h at operating temperature and pressure (hereafter OTP) of 9 °C and 2 bar, except in the case of the (iv) SED with OTP of 27 °C and 1 bar, and the (v) SED with OTP of 1 bar over a temperature range of 5–13 °C.

All results were obtained using standard SIMPLE instrumentation, comprising a single electret microphone with 0–16 kHz sensitivity, without amplification or filtering. Analysis was also standard, using the natural logarithm of the squared amplitude of the principal harmonic of the power density spectrum (ln(K)) for each event with frequency 450–750 Hz and decay constant of $5-40$ ms [34].

The measured power distribution of the irradiation sequences are shown in Figs. 2–5, with the “(a)” displaying the neutron-then-α irradiations, and the “(b)” the α-then-neutron irradiations; each response distribution was normalized to unity:

Case (i). the results shown in Fig. 2(a), comprising 794 recoil and 532 α events, indicate the existence of the gap between the recoil and α power distributions. The α distribution is asymmetric tailing to higher powers. In Fig. 2(b), with 672 recoil and 631 α events, the recoil distribution is virtually identical to that of Fig. 2(a). In comparison with Fig. 2(a), the α distribution is significantly broadened in its lower power structure, with its peak shifted downwards to ln(K) $= 9.5$. The two response distributions are almost separated.

The apparent shift of the neutron distribution in Fig. 2(a) from that of previous measurements [4] with a 900 ml science detector

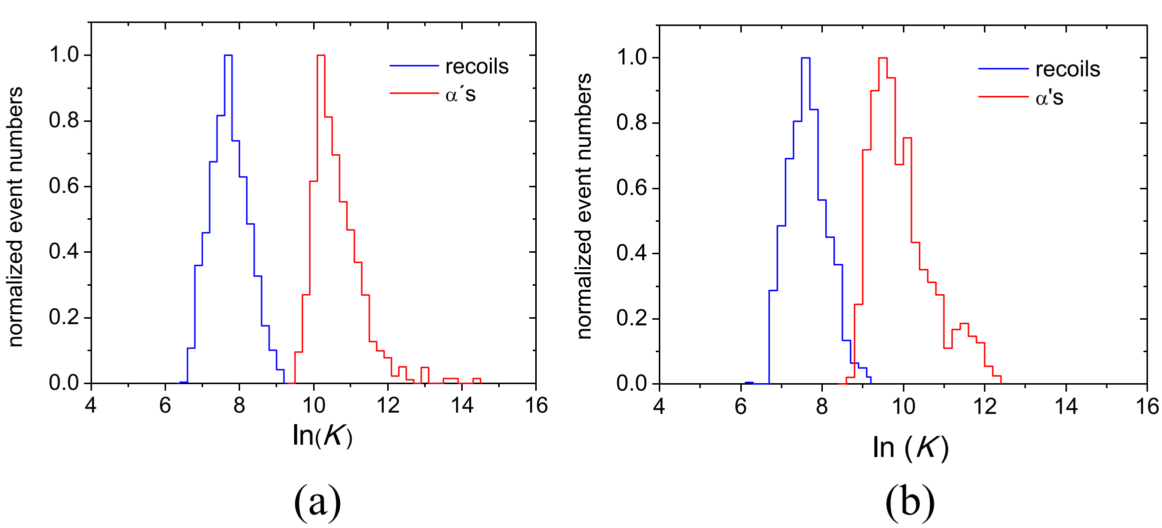

Fig. 2. Recoil- and α-induced event power distributions for (a) neutron-then-α and (b) α-then- neutron irradiations.

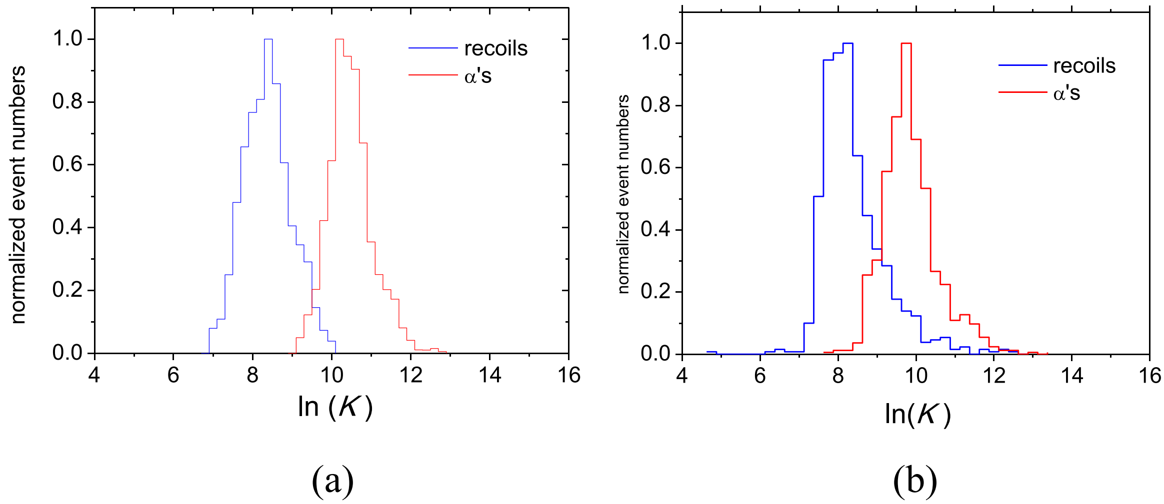

Fig. 3. Recoil- and α-induced event power distributions as in Fig. 2: big droplet distribution.

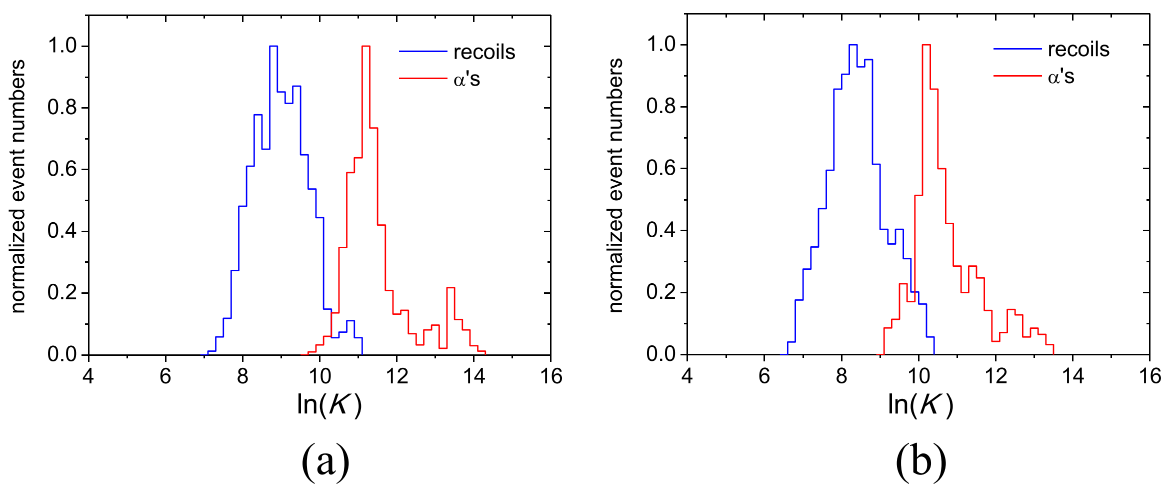

Fig. 4. Recoil- and α-induced event power distributions: stiffer gel SEDs.

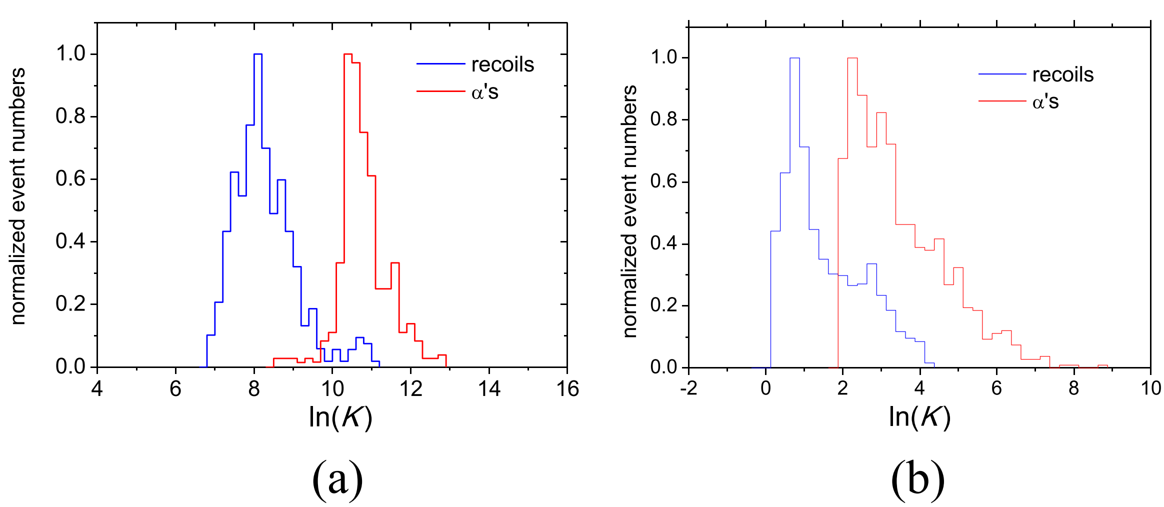

Fig. 5. (a) Spectra of recoil- and α-induced event power distributions: C_4F_{10} SED at 27 °C/1 bar, with stiffer gel and $\langle r\rangle\sim$ 23 μm; (b) C_2ClF_5 SED at 9 °C/1 bar, $\langle r\rangle\sim$5.5 μm.

is a result of the smaller SED size, and pressure wave attenuation. The mean of the sound distance in the larger device was ~5 cm, vs. the 4 cm of the devices herein, yielding an amplitude increase of ~20% to peak at ln(K) =7.5.

Case (ii). in contrast toCase (i), the neutron-then-α result in Fig. 3(a), comprising 727 and 607 events, indicates an increased overlap of the two power distributions. The recoil distribution is shifted to higher power, while the peak of the α distribution remains

Table 1
Summary of single detector variations and irradiation results for nuclear recoil and α distributions. Unless otherwise noted, the liquid is C_2ClF_5.

Case	Fig.	Description	Recoil distribution ln (K_{min}) – ln (K_{peak}) – ln (K_{max})	α distribution ln (K_{min}) – ln (K_{peak}) – ln (K_{max})	% overlap
(i)	2(a)	< r > ~10 μm; std gel	6.5 – 7.5 – 9.2	9.7 – 10 – 12	0
	2(b)	< r > ~10 μm; std gel	6.5 – 7.5 – 9.2	8.8 – 9.5 – 12	1.56
(ii)	3(a)	< r > ~23 μm; std gel	6.9 – 8.3 – 10	9 – 10 – 12	0.82
	3(b)	< r > ~23 μm; std gel	7 – 7.9 – 12	8 – 9.7 – 12	12.5
(iii)	4(a)	< r > ~10 μm; stiff gel	7.2 – 9 – 10.2 + 11	10 – 11.2 – 12.5 + 14	6.07
	4(b)	< r > ~10 μm; stiff gel	6.5 – 8.2 – 10.2	9 – 10.2 – 12 + 13.5	9.65
(iv)	5(a)	< r > ~10 μm; stiff gel, C_4F_{10}	6.9 – 8.2 – 10 + 11	9 – 10.4 – 13	21.1
(v)	5(b)	< r > ~5.5 μm; std gel	~0 – 0.8 – 4.3	2 – 2.2 – 7.5	18.9

virtually unaltered with a slight decrease in its low power tail to overlap the high power tail of the recoil response. The histogram of the reversed irradiation sequence (770 recoil and 598 α events), is shown in Fig. 3(b): the α response peak is similar to Fig. 2(b) but its low power tail reaches to ln(K) ~8. The recoil distribution, no longer symmetric, exhibits a high power tail spanning the α distribution, with its peak now shifted downward to ln(K) ~ 7.8 as in Fig. 2(b). The recoil response is slightly higher than Figs. 2(b) or 3 (a); the α response, slightly lower than either.

Case (iii). Fig. 4(a) comprises 480 recoil and 570 α events. Both responses are shifted upwards in power relative to Fig. 2(a), with the exception of the lower limit of the α-response. The α-distribution is seemingly narrower, and accompanied by a secondary high power component. The recoil distribution is of higher power than either Figs. 2(a) or 3(b), as also the α-distribution with respect to Figs. 2(b) or 3(b); it appears somewhat broadened, but in fact remains contained between ln(K) =7–10. Both distributions overlap, and include high power tails. In Fig. 4(b), comprising 281 neutron- and 453 α-induced events, the α peak has returned to that of Fig. 3(a), with the principal distribution again seemingly narrower and accompanied by a significant low power tail. The recoil distribution is broader than in Fig. 2(b) as a result of an enhanced high power tail.

Case (iv). the results of the neutron-then-α irradiations (364 recoil and 231 α-events) are shown inFig. 5(a). The two power distributions are clearly non-coincident, the results being similar to those of both Figs. 3(a) and 4(b). There is no significant overlap of the primary response distributions, the small overlap arising from the high power recoil response tail which extends well into the α distribution.

Case (v). the α-then-recoil response at 9 °C and 1 bar (909 α and 874 recoil events) is shown in Fig. 5(b). Both power distributions are asymmetric as in Fig. 2(a), and of lower power relative to both the α- and recoil responses of Figs. 2–4; the α response is of higher power than the recoil event, unlike the results of Ref. [11].

Table 1 contains a summary of the SED characteristics and observed power distribution parameters.

In all cases, the results manifest a clear separation between recoil and α-induced event peaks. With the exception of Case (i), there is generally a partial overlap of the low power α and high power recoil distributions. The recoil spectra of the "(b)" Figs. include the simultaneously occurring α-decay during the neutron irradiations which contribute to the higher power tails. In Case (ii), all α distributions generally appear symmetric, as also the recoil response of Fig. 3(a) whose peak power has also risen slightly relative to Case (i). In Case (iii), the α distributions appear narrower, whereas the recoil distributions appear broader. The results of Case (iii) manifest structure in the higher power region of the α-event distributions.

Previous studies [35] with different droplet size distributions, gel stiffness and mixed irradiations have shown that the observed signal amplitudes of a larger droplet size distribution are uniformly larger than a smaller-sized as might be expected from Eq. (2). Larger droplet size expansions are also accompanied by an increased probability of sympathetic bubble nucleations which can combine to yield increased signal amplitudes.

With stiffer gels, the signal amplitudes are also larger than with the "standard" gel [35]. One might think that the decreased gel elasticity would restrict the range of bubble expansion relative to the less stiff, resulting in narrower power distribution. This is observed for the α-irradiation, but not for the recoil event distribution. In Case (iv), with an increased operating temperature of 27 °C, the gel becomes more liquid and the signal amplitudes increase since there is less resistance to the bubble expansion.

The liquids themselves (as well as of Ref. [11]) are not significantly different in their characteristic properties, as seen in Table 2.

Apart from the obvious differences in instrumentation, the experiments also differ in their measurement observable. The total energy release in a bubble nucleation is the superheat of the droplet: for C_4F_{10} at 1 bar and 27 °C, E_{total}~2.1×10^{-8} J, well in excess of a 10 MeV energy deposition (1.6×10^{-12} J). Although only a fraction of the energy appears in the acoustic signal, the same–sized droplet releases the same energy whether triggered by α or recoil interactions. For comparison purposes, we convert Fig. 5 (a) from ln(K) to $AP = \log\left\langle \int_0^\tau A^2 dt \right\rangle$ via $\int_0^\tau A(t)^2 dt = \int_0^\tau A_0^2 e^{-2t/\lambda_j} dt \sim A_0^2(\lambda_j/2)$, with j =(recoil, α), the λ's taken from the signal analysis, and normalizing the AP of the recoil mean to 1. The result, in Fig. 6 (a), yields an overlap of the two event distributions, in reasonable agreement with Fig. 10 of Ref. [7] at 27.5 °C, as also the salient features of each distribution with the exception of the inverted tail structure of the α distributions. The same analysis applied to the data of Fig. 2(a) yields Fig. 6(b) which preserves both the shapes of the event distributions and the peak separations but not the gap, suggesting that the α distribution derives from larger droplets of larger r than the recoil response.

Table 2
Properties of the three liquids mentioned herein, calculated using tabulated values of σ, ρ_v, h_v [36–38]. In the case of C_2ClF_5, the OTP entries are for 9 °C/2 bar; for C_4F_{10}, 27 °C/1 bar; for CCl_2F_2, 33.5 °C/1 bar [11].

Liquid	T_c (K)	p_c (kPa)	T_b (K)	ρ_l-OTP (g cm^{-3})	E_c-OTP (keV)	R_c-OTP (μm)	s-OTP
C_2ClF_5	353.1	3158	250.8[a]	1.37	7.8[a]	0.0341[a]	0.31
C_4F_{10}	386.3	2289	271.4[b]	1.49	42.1[b]	0.0749[b]	0.25
CCl_2F_2	385.0	4136	243.4[b]	1.27	3.10[b]	0.022[b]	0.45

[a] 2 bar.
[b] 1 bar.

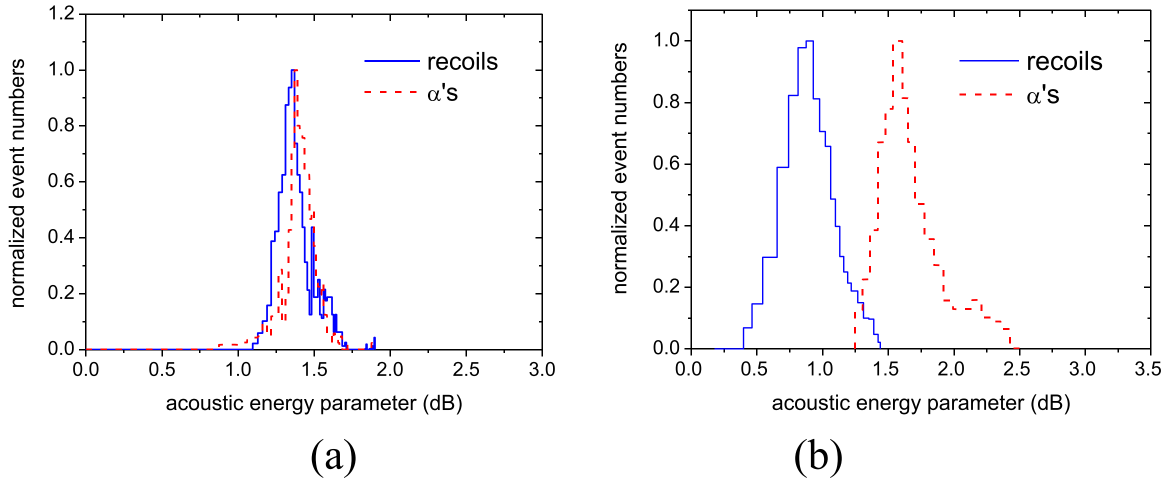

Fig. 6. Reanalyzed power spectra in terms of AP for (a) Figs. 5(a), (b) and 2(a).

4. Analysis

Since larger droplet size distributions and gel stiffness are common to both irradiations, there is no obvious differential to provide the difference between the two response distributions. We examine the incident radiation interaction and nature of the particle energy loss in the liquids.

4.1. Neutron-induced nuclear recoil events

Elastic neutron scattering on target nuclei provides nuclear recoils with the maximum recoil energy (E_R) of an ion A given by $E_R{}^A = \omega_A E_n$, and $\omega_A = \frac{4A^2}{(1+A)^2}$: $\omega_C = 0.28$, $\omega_F = 0.19$, and $\omega_{Cl} = 0.11$. For the AmBe source, the incident neutron energy E_n ranges to 10 MeV, yielding $E_R{}^C \leq 2.8$ MeV, $E_R{}^F \leq 2$ MeV and $E_R{}^{Cl} \leq 1.1$ MeV. In the reactor irradiations ($E_n < 300$ keV), recoils with maximum $E_R{}^C = 84$ keV, $E_R{}^F = 57$ keV, and $E_R{}^{Cl} = 33$ keV are obtained; at OTP, $E_c{}^{Cl} = E_c{}^F = 8$ keV and $E_c{}^C = 120$ keV, so that carbon ions are unobserved.

Inelastic scattering also generates nuclear recoils for neutron energies above the reaction threshold (120 keV for F, 1.3 MeV for Cl and 4.8 MeV for C). However, the contribution of these reactions is very reduced, as the neutron moderation by the SED hydrogenous gel matrix down scatters the incident neutrons to energies below the reaction threshold [39]. Among transmutation reactions with positive Q-value, $^{35}Cl(n,p)^{35}S$ and $^{35}Cl(n,\alpha)^{32}P$ are in principle of interest because the emerging ions have a minimum energy of 17 keV (^{35}S) and 104 keV (^{32}P) that can provoke a bubble nucleation. These reactions however have cross sections smaller than those of elastic scattering in Cl by ~1–7 orders of magnitude, and their contribution to the detector signal is generally small (with exceptions in thermal neutron fields). There are also high LET Auger cascades from environmental γ interactions with the Cl, with a threshold of ~16 °C at 2 bar, which prescribes its operation at lower temperatures.

Fig. 7(a) displays track-averaged Bragg curves calculated using SRIM [40] at OTP for fluorine ions of various initial $E_R{}^F$ in C_2ClF_5; the 0-depth entry equals the stopping power at $E_R{}^F$. The inset, displaying the 5–100 keV recoils, indicates the C_2ClF_5 LET_c to be exceeded over penetration depths of ≤ 0.4 μm, significantly below the smallest droplet sizes and $\sim 10 \times L_c$; the lighter carbon ions penetrate larger depths due to their higher recoil energies and smaller stopping power. The higher E_R of AmBe-generated recoils range up to 2.8 MeV with LET > > LET_c, calculated from the data of Table 2 and $\Lambda_{C2ClF5} = 1.40$ [41]. For C_4F_{10}, the situation is somewhat different as seen in Fig. 7(b), which shows several track-averaged recoil F ion Bragg curves in C_4F_{10} at 27 °C, together with the LET_c

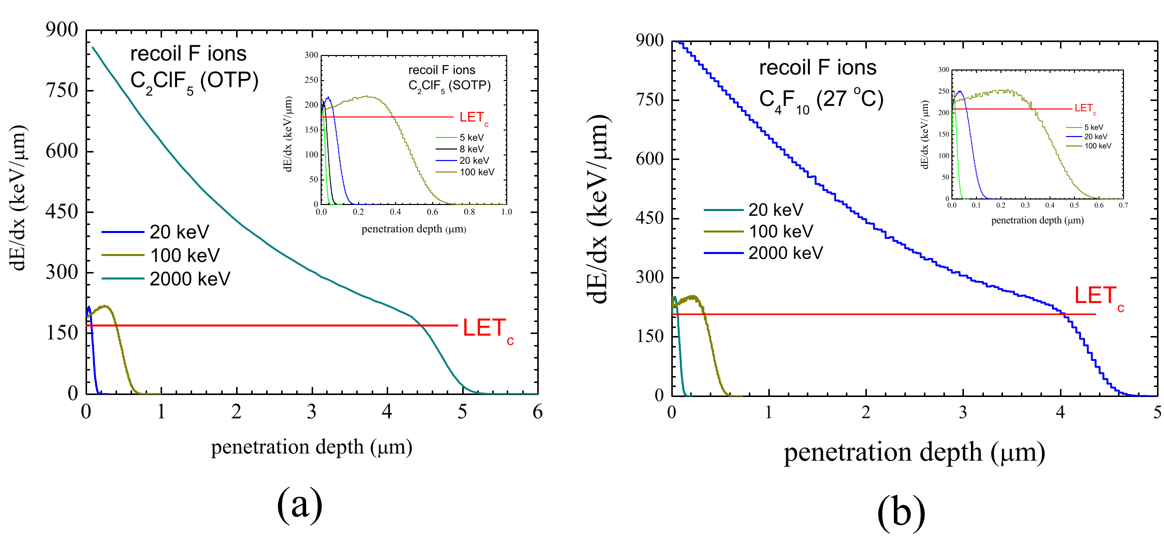

Fig. 7. (a) Bragg curves of recoil fluorine ions of various initial energies in C_2ClF_5 together with the LET_c; (b) same for fluorine recoils of 5, 20 and 100 keV in C_4F_{10} at 27 °C.

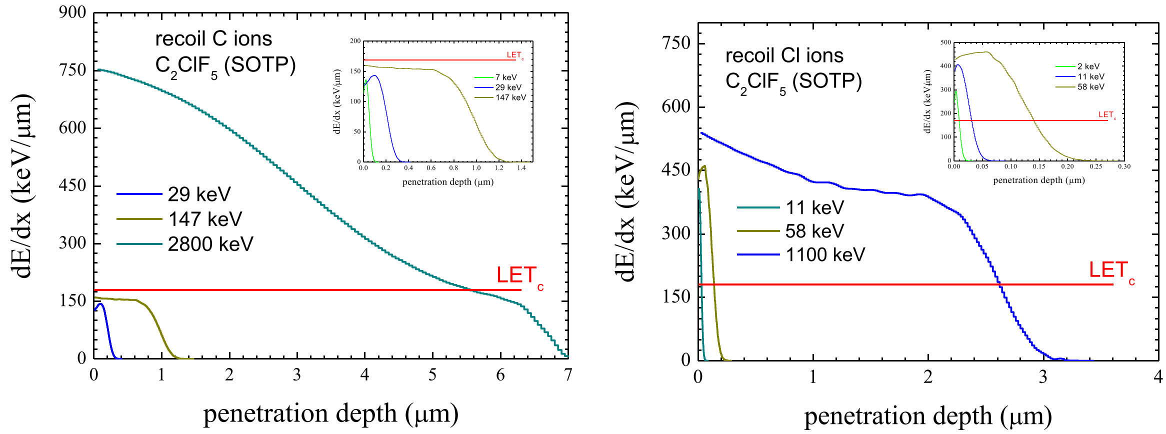

Fig. 8. (a) Bragg curves of recoil carbon ions of various initial energies in C_2ClF_5 together with the LET_c; (b) same for chlorine in C_2ClF_5.

derived from Fig. 6 of Ref. [7] and respective $E_c(T)$, $r_c(T)$. The profiles are generally similar to Fig. 7(a) inset, but range to ~ 0.07 μm, with $LET > LET_c$ over distances of ≤ 0.04 μm $\sim r_c$.

For comparison, Fig. 8 display the Bragg curves for carbon and chlorine recoil ions, calculated with the recoil energies corresponding to the same incident neutron energies of Fig. 7(a).

The neutron mean free path with $E_n = 10^{-8}$–10^{-1} MeV is $\sim$0.2–0.3 cm, far larger than the largest droplet diameters: subsequent elastic scatterings occur in the gel or other droplets. For the low energy recoils, the track-averaged path lengths for which $LET > LET_c$ are of order L_c, and O(1) proto-bubble formation is anticipated; increased proto-bubble production is expected for the higher energies.

4.2. Alpha decay events

For U_3O_8, the main α decay energies are $E_\alpha = 4.2$ and 4.7 MeV [42]. Although an α decay is itself a "recoiling" ^{4}He ion, its larger kinetic energy produces a significantly different track-averaged Bragg curve relative to a target ion recoil (Fig. 9). As indicated, α's originating on a droplet surface would generally achieve $LET > LET_c$ in C_2ClF_5 over several microns in the liquid following several tens of microns penetration with $LET < LET_c$. Droplets with diameters less than a minimum penetration distance $p_<$ cannot support bubble nucleation since the α transits the droplet without achieving LET_c.

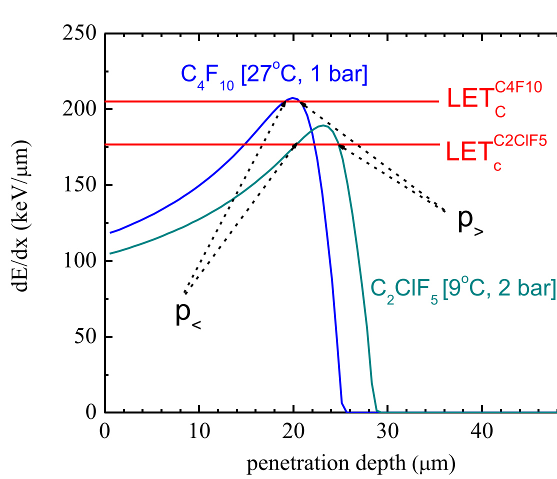

Fig. 9. SRIM-computed Bragg curves for 4.0 MeV α's in C_2ClF_5 and C_4F_{10} at their OTPs. The respective LET_c, obtained from Refs. [5,6] are also indicated. The $p_<$, $p_>$ define the track-averaged penetration depths for each, between which the dE/dx $\geq$ LET_c.

The situation appears significantly different for C_4F_{10}, where the maximum of the Bragg peak is virtually coincident with the LET_c.

The energies of the ^{238}U and ^{234}U daughters are 86 keV (^{230}Th) and 72 keV (^{234}Th) [42]. These have penetration depths of $\sim$0.10 μm, 0.08 μm of which exhibits $LET > LET_c$: in contrast to the α, the daughters behave more like the target recoils of Figs. 7 and 8 and can mimic a recoil event.

4.3. Alpha-recoil event separation

From the experiments of Section 2, two aspects seem evident: (1) the same droplet size distribution produces two different acoustic responses, and (2) the acoustic response profiles of each are different. The first is addressed from the above: it is clear that α's (as well as high energy nuclear recoils) in general have a higher proto-bubble generation capacity. Each proto-bubble formation within a droplet serves as an evaporation center, and the droplet evaporation time is accordingly reduced to τ_0/n_j, where n_j is the number of proto-bubbles created by radiation type j, and τ_0 is the droplet evaporation time for $n_j = 1$.

Since the bubble and droplet have the same mass, $r_b = (\rho_l/\rho_v)^{1/3} r_d$, and Eq. (2) can be re-expressed in terms of r_d as

$$K = A_0^2 r_d^6 n_j^4, \tag{5}$$

with $A_0^2 = 4\pi\rho_l(\rho_l/\rho_v)^2 c^{-1}\tau_0^{-4}$. With $n_r = 1$, the recoil signal distribution should then mirror the droplet size distribution. This is observed experimentally, as seen in Fig. 10 [5]. Moreover, for the same droplet size, the n_α^4 serves as an amplification factor for separating the two particle-induced acoustic power responses if the α proto-bubble formation is sufficiently > 1.

As an example, consider Fig. 2(a) in which:

$$\ln(K_r|^{max}) = \ln(A_0^2 r_{d\,max}^6 n_r^4) = 9.2, \tag{6a}$$

$$\ln(K_\alpha|^{min}) = \ln(A_0^2 r_{d\,min}^6 n_\alpha^4) = 9.7. \tag{6b}$$

Assuming for the sake of argument that $n_r = 2$ with the measured $r_{dmax} = 22$ μm, $r_{dmin} = 11$ μm from Fig. 9, $A_0^2 = 5.456 \times 10^{-6}$ from Eq. (6a) and $n_\alpha = 6.4$ from Eq. (6b), consistent with the results of Diemand et al. [43]. A similar analysis of the partial separation of the α and recoil peaks in Fig. 5(a) with $r_{dmax} = 40$ μm and $2r_{dmin} = 38$ μm for the C_4F_{10} with $n_r = 2$ (1) gives $A_0^2 = 3.361 \times 10^{-7}$ (5.378×10^{-6}) and $n_\alpha = 4.8$ (2.4) in agreement with Ref. [7]. The increased proto-bubble formation in α-droplet interactions amplifies the acoustic signal amplitudes above those of the recoil.

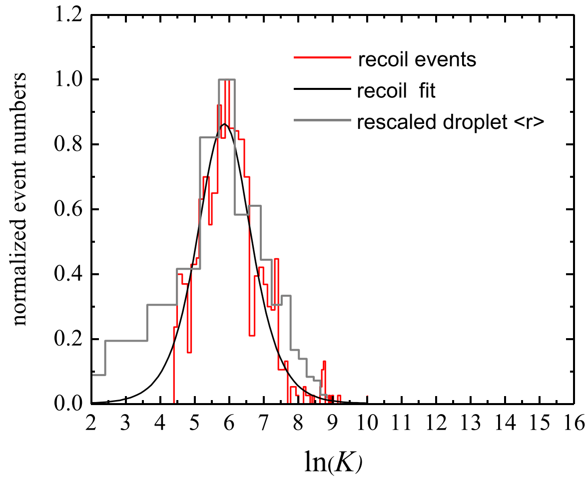

Fig. 10. Power analysis of recoil events generated by neutron irradiation (solid), in comparison with a droplet size distribution (dashed) generated by the "standard fabrication protocol" when scaled as A ~ $\xi r^3$with ξ^2 adjusted to overlap the two distributions (accounting for A_0^2). [5].

4.4. A simple response model

The question of differing acoustic distribution profiles is addressed via a "surface emission" model, based on Pan et al. [19] which can be used to estimate the anticipated response of SEDs to actinide doping, such as ^{241}Am or U_3O_8. In this case, the atoms have an electrochemical affinity for both C_2ClF_5 and C_4F_{10} molecules, as also do the complex ions with which they are normally associated [44–46]. In consequence, they should migrate towards the droplet surfaces to preferentially populate the larger droplet surfaces; at the least, larger droplets should have a larger number of α-emitters, hence higher decay probability. A surface origin for the α emission is not unreasonable [47], since the ions are affinic to the hydrophobic surface of the droplets. In fact, the complex ions themselves stabilize the emulsion by acting as a surfactant [46].

Assuming surface emission, only α's entering the shaded region of the droplet shown in Fig. 11(a) produce proto-bubbles, where $p_<$, $p_>$ demarcate the penetration depths of the Bragg curves over which the LET > LET_c (see Fig. 9). A bubble nucleation probability, automatically reduced to < 50% by the α isotropic emission, is obtained by subtracting the volume intersection ($V_<$) of the droplet sphere with a sphere of radius $p_<$ centered at the droplet radius, and normalizing to the droplet volume: $P_{bn}(r) = \frac{1}{2}$ (V_d -$V_<$)/V_d, where

$$V_< = \frac{\pi p^2(8pr_d - 3p^2)}{12r_d}. \tag{7}$$

Similarly, an α proto-bubble generation probability (P_{pb}), corresponding to the region of the Bragg curve between $p_<$ and $p_>$(i.e. with LET > LET_c) is obtained as $P_{pb}(r) = \frac{1}{2}$ [(V_d- $V_<$)−(V_d- $V_>$)]/V_d= $\frac{1}{2}$ [$V_>$- $V_<$)]/V_d. For the 4.2 MeV α's of the Section 3 experiments, droplets with 2r < $p_<$ =22 μm do not support proto-bubble formation; those with 2r > $p_>$ =25 μm do not contribute further proto-bubbles since the α LET is below LET_c. Shown in Fig. 11(b), P_{bn} rises from zero at 11 μm to asymptotically approach 0.5 with increase in r_d; for droplets with r > 12.5 μm, no further proto-bubble formation occurs and P_{pb} decays. Given our interest in the signal production as a measure of the SED response, we neglect P_{pb} in the discussion hereafter.

The neutron-generated recoil signal is biased by the inherent geometric cross section of droplet size. As noted previously [5], the larger the droplet, the more likely is a scattering, and the recoil window is initially populated by high amplitude events. This is seen in Fig. 12 taken from the data of Fig. 2(a): the first recoil events include amplitudes reaching to near 100 mV, although these rapidly drop to cluster above the mean of A=43 mV. As the droplet depopulation progresses, the mean of the recoil event distribution first shifts downward, then rises to the mean of the Fig. 2(a) distribution, accompanied by the disappearance of events with A > 60 mV.

Measurements of pristine, α-doped detectors in contrast show no time-ordered droplet size-related geometric interaction probability, as seen in Fig. 12(b) taken from the data of Fig. 2(b). The lowest power α-event occurs only after 125 previous events, with the bulk of event ln(A^2) ≥ 9.7. The event spectrum however suggests that only the upper half of the droplet distribution is involved. Note that the (a) spectrum slope from event 20–150 is about that of the (b) spectrum minimum, giving possible evidence of an expected [49] sound attenuation with increase in bubble populations and/or larger droplet depletion. Note however that initial neutron irradiation tends to remove the larger droplets first, so that the α doping is relegated to the smaller – which is the greater interest with respect to particle response discrimination since it likely relates to the gap between the two distributions observed in Fig. 2(a).

Given the above, the original droplet size distribution is modified by a geometric cross section factor $\varepsilon_g = \left(\frac{r_d}{r_{max}}\right)^2$ to N'(r)=P_{bn} ε_g N(r), as shown schematically in Fig. 13 for a normalized Gaussian distribution of < r_d > =15 ± 5 μm, with P_{bn} computed for

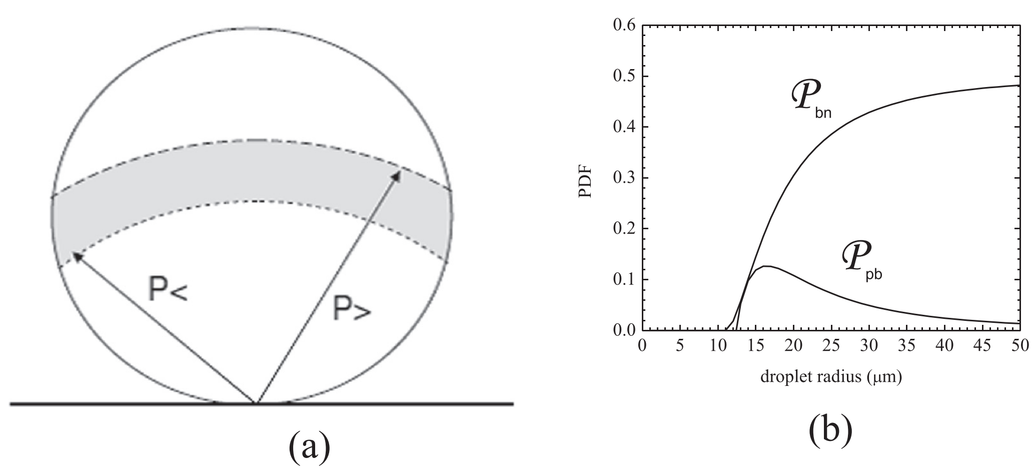

Fig. 11. (a) Scenario of the "surface emission" model: only α particles originating from the droplet surface emitted into the shaded spherical volume may contribute; (b) variation of P_{bn} and P_{pb} with droplet radius for a Gaussian < r > =15 ± 5 μm distribution.

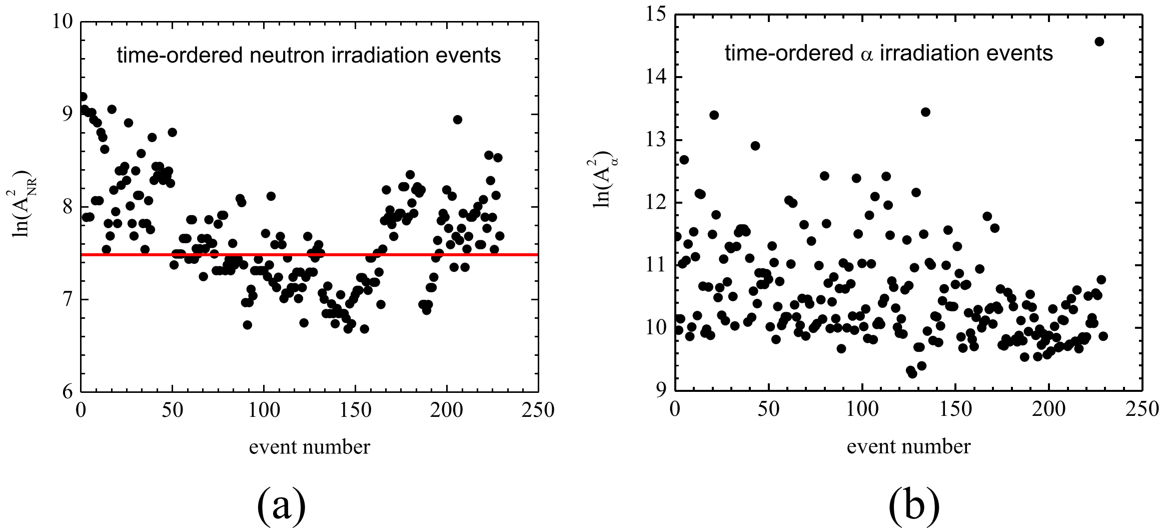

Fig. 12. Typical scatter plot of the first 230 recorded event amplitudes in neutron irradiation (a) and α irradiation (b) of a SED, indicating the exposure-dependent populating of the eventual recoil distribution.

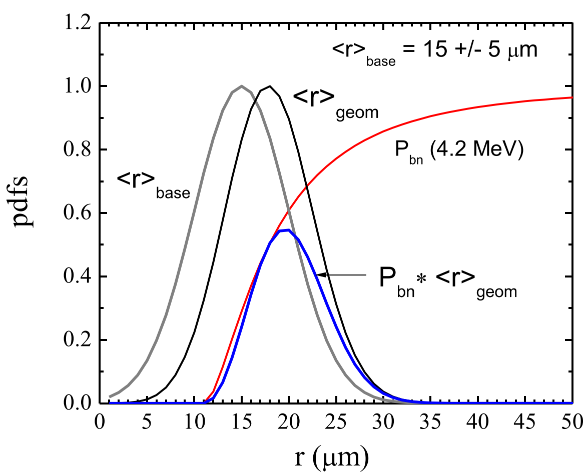

Fig. 13. Model interaction of a Gaussian droplet size distribution of $<r> = 15 \pm 5$ μm with 4.2 MeV α's ($p_< = 11$ μm).

$E_\alpha = 4.2$ MeV. The gray contour represents the initial gaussian distribution; the black, its geometric-correction. The red curve is P_{bn}, and the purple is the un-normalized convolution result. As evident, for diameters below the $p_<$ cut, the droplets are insensitive to the α's: the irradiation samples only the upper half of the SED droplet sizes. Higher energy α detection requires larger droplet sizes or distributions.

Fig. 14(a) displays the anticipated "acoustic power response" of 4.2 MeV α's incident on SEDs with geometrically-weighted Gaussian size distributions of the several $<r_d>$ of this study, now cast as a function of $\ln(r_d^6)$: the amplification factor n_α^4 is neglected in order to examine the effect of P_{bn} on the resulting response, and the result un-normalized to indicate its relative strength. For droplet size distributions with $<r_d> \leq p_<$, the probability cut samples only the large radius tail of the distribution, yielding an asymmetric response distribution which becomes increasingly symmetric as $<r_d>$ increases. As $p_<$ increases, the sensitivity of the small droplet distributions vanishes.

Note that the two smallest of the five considered $<r>$ distributions do not appear in Fig. 14(a), since the $P_{bn} \sim 10^{-8}$–10^{-4}.

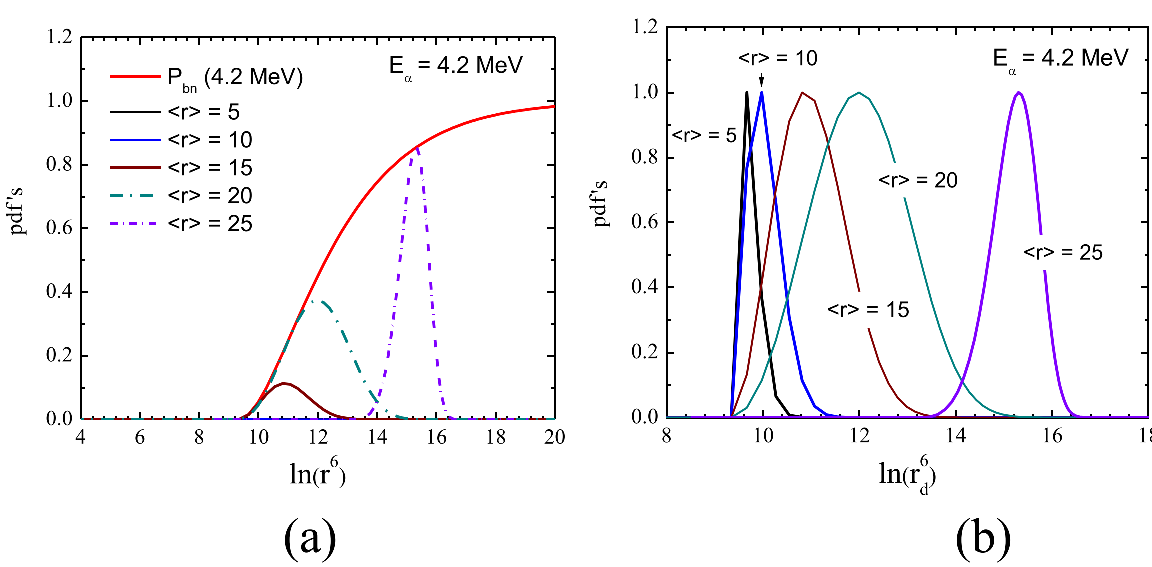

Fig. 14. (a) convolution of the bubble nucleation efficiency with Gaussian droplet size distributions of $<r_d> = 5 \pm 3$, 10 ± 3, 15 ± 5, 20 ± 7 and 25 ± 8 μm and $E_\alpha = 4.2$ MeV; (b) same as (a) but with the simulated response now normalized.

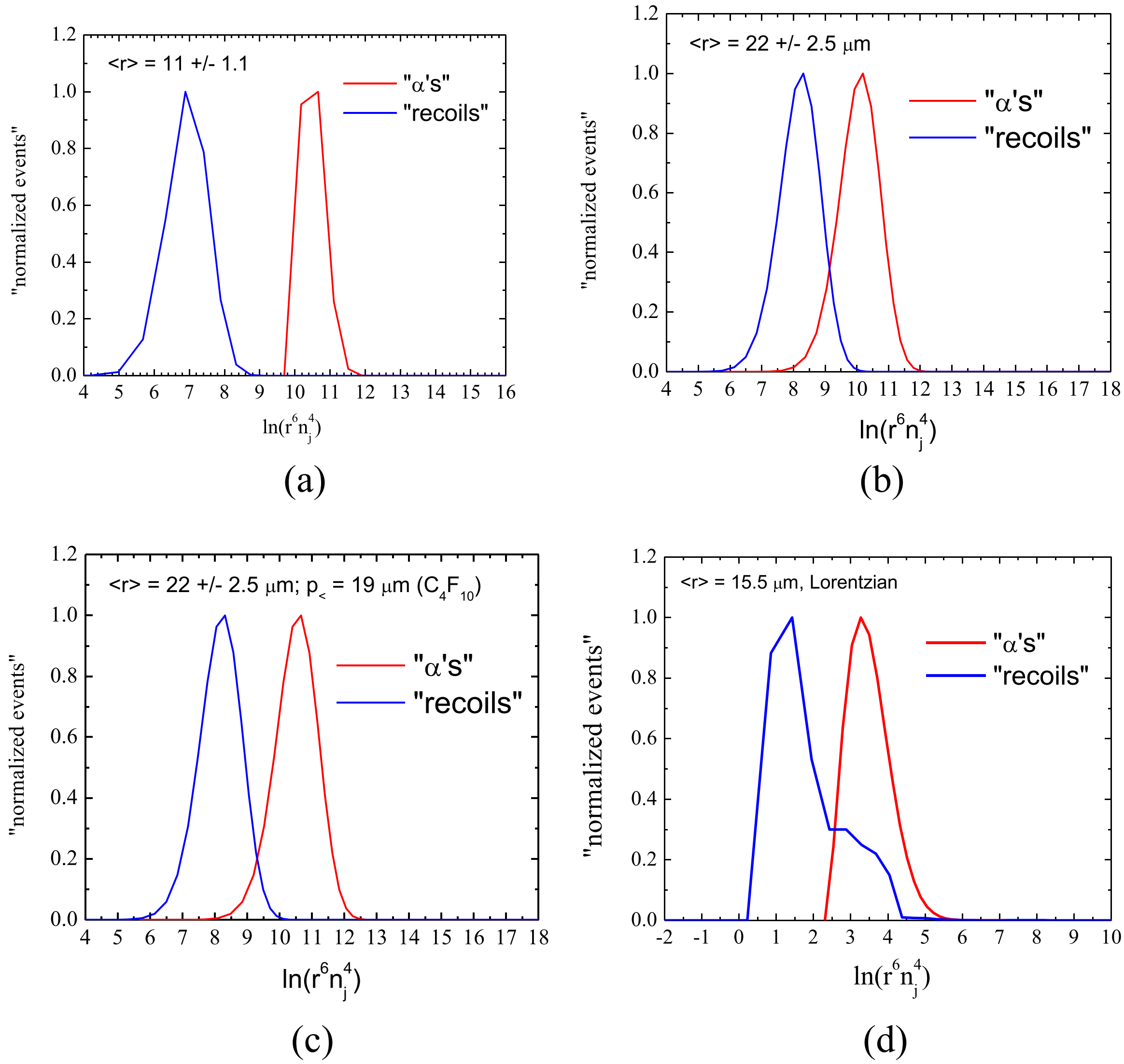

Fig. 15. results of the model described in the text, with $A_\alpha^2 = \xi^2\, r_d^6\, n_j^4$ and ξ^2 adjusted to overlap the recoil response with its respective experimental result, for comparison with (a) Figs. 2, (b) Fig. 3, (c) Fig. 5(a), (d), (b).

Given that the SED may however contain upwards of 2×10^8 droplets in its distribution, events will occur which manifest themselves in a normalized presentation. Fig. 14(b) displays the Fig. 14(a) results now normalized (as generally presented in calibrations). As evident, the smallest $<r>$ responses are highly asymmetric since only the large r tail of the distribution is being sampled; as $<r>$ increases above $p_<$, the α response becomes increasingly symmetric.

Since the decay daughters also share the droplet surface origin, the reverse considerations apply with $p_< = 0.1$ μm: the contribution is a priori reduced by 50%, but essentially 100% otherwise. The contribution from α-emitters outside the droplets is estimated at $< 1.5\%$ [48, 49].

The results of the model for the Section 3 experiments are seen in Fig. 15 with daughter contributions neglected. Fig. 15 (a) corresponds to Case (i): the recoil distribution is obtained by rescaling the abscissa as $A^2 -> \xi^2 r^6\, n_r^4$ with $n_r = 1$ and adjusting the abscissa by $\xi^2 = -7.5$ to overlap the recoil distribution of Fig. 2(a). The α distribution is similarly obtained, with $n_\alpha = 0$ for $r_d \leq 11$ μm and $n_\alpha = 1.6$/μm for $r > 11$ μm; the same ξ^2 shift is employed. The observed gap between the two and asymmetry in the α distribution of Fig. 2(a) is indicated.

Fig. 15(b) corresponds to Case (ii), with the $< r_d > = 22 \pm 2.5$ μm droplet size distribution, $p_<$ obtained from Fig. 9 and $n_\alpha = 1.6$ regardless of size above $r_d = 11$ μm. The event distributions are overlapped, as seen experimentally.

Fig. 15(c) corresponds to Case (iv), with the $< r_d > = 22 \pm 2.5$ μm size distribution, $p_< = 19$ μm obtained from the C_4F_{10} Bragg curve of Fig. 9 and $n_\alpha = 1.8$ regardless of size above $< r_d > = 9.5$ μm. Although the simulated α event distribution exhibits the same structural symmetry as Fig. 15(b), the response overlap is decreased; the lower $p_<$ is apparently compensated by the n_α of C_4F_{10}.

Fig. 15(d) corresponds to Case (v), with the experimentally-measured $< r_d > = 5.5$ μm droplet size distribution approximated by a Lorentz distribution tailing to ~16 μm, $p_<$ from Fig. 9 and $n_\alpha = 1.6$/μm for $r_d > 11$ μm. Both simulated event distributions occur at a significantly reduced power and exhibit the structural asymmetry of the experimental results; the recoil power distribution however remains below that of the α, in contrast to Ref. [11].

5. Summary

The acoustic response of SEDs to nuclear recoil and α events is seen to fundamentally depend on the relation between the incident particle energy and distribution of droplet size in the detector. Low energy nuclear recoils of the target nuclei yield an O (1) proto-bubble formation, as also the α-decay daughters; α's and high energy recoils, generally more. Each proto-bubble is formed on time scales less than for a complete bubble nucleation event, hence serves as an additional evaporation center for the bubble nucleation, providing an amplification factor to the acoustic signal power.

In the case of actinide α-doping, the SED response can be estimated via a simple model based on the intersection of two spheres, one a droplet and the other of radius $p_<$ obtained from the intersection of the particle Bragg curve with the LET_c of the liquid at its OTP. The model is seen to address the profile variations via the droplet size distribution and incident α energies. As seen for Gaussian droplet size distributions with means $\langle r \rangle$ below $p_<$, the α-response is asymmetric in its lower amplitudes since the α's sample only the larger droplets of the distribution. As the distribution mean increases above $p_<$, the response becomes increasingly symmetric as more of the smaller droplets become involved. The apparent decrease in power of the α response in Case (ii) is a result of the increased distribution $\langle r_d \rangle$ above the $p_<$ of the U_3O_8. The model is usable with all droplet distributions and actinide α-emitters; applied to the results of Section 3, it reproduces well the experimental results.

The model is not directly applicable to the observations of Ref. [11] since the α irradiation is initiated external to the SED and hence more properly relates to α surface emission from the SED containment walls. It does however provide some further insight into the results, which are attributed by the authors to the smaller n_α formation resulting from partial α passage through the $\langle r1 \rangle$ distribution. As seen from the Bragg curves of Section 4, proto-bubbles are generated only when the α $dE/dx \geq LET_c$: this range is reduced compared to the full particle range in the droplet liquid. The proto-bubbles moreover serve as triggers to the bubble nucleation: the total acoustic energy release of a droplet, which is the P variable of Ref. [11] (and not the signal power) is $\sim r_d^6$, and the signal amplitude differences depend only on the relative difference in the $\langle r1 \rangle$, $\langle r2 \rangle$ sizes. The n_α=range/L_c of Ref. [11] is questionable, as also that $L_c = E_c/(dE/dx)$, since the denominator obtained from the stopping power curve reflects only the zero-thickness value of the respective Bragg curve. The more likely explanation of the apparent response inversion is that the ^{241}Am α's, degraded by their air passage, must transit ~11 μm of glycerol before their dE/dx approaches the CCl_2F_2 LET_c at OTP – droplets within this distance are effectively blind to α's, and the α response must come entirely from the $\langle r1 \rangle$ droplets within an approximately hemispherical shell of ~17 μm thickness at a 11 μm distance from the SED-air interface, in contrast to the neutron irradiations which sample the entire SED droplet population (in particular $\langle r2 \rangle$ with larger geometrical cross section).

The simple model neglects a number of presumably higher order effects including α-emission outside the droplet, ion straggling and nucleation efficiencies, and can therefore only be considered a first approximation. Also not covered by the present model is the case of non-actinide α-emitter doping in which the decay daughters may diffuse into the droplets. This is to be addressed in a forthcoming paper. Despite this, the above description is consistent with observations, and captures the essence of the involved response physics in SED devices. The sensitivity of a detector to the range of decay E_α is clearly dependent on the distribution of droplet size in the device, requiring careful characterization measurements and establishment of fabrication protocols for reproducibility.

The question of recoil - α acoustic power separation is dependent on a gap existence, hence whether the n_α^4 amplification factor is sufficient to promote the lower power tail of the α response above the high power tail of the recoil response. The principle problem is the estimation of proto-bubble formation probability, which is far from clear. The $P_{pb}(r)$, not discussed herein, describes only the droplet sensitivity to multiple proto-bubble formation and gives only the droplet volume capable of supporting proto-bubble formation, not the number per micron. As seen by the particle Bragg curves, the number of proto-bubbles generated by particle interactions depends on the dE/dx of the particle in the target liquid, and its relation to the LET_c of the fluid at OTP. In the case of C_2ClF_5, the LET_c is well-below the Bragg peak, providing α proto-bubble formation probabilities over 5–15 μm of penetration; for C_4F_{10}, LET_c is at or just below the maximum of the Bragg peak. The simulation of Figs. (b) and (c) however support similar n_α's. The difficulty in defining the LET_c of a liquid derives from the presence of Λ in Eq. (3), and use of the stopping power curves in its determination since the dE/dx from the latter at a given incident energy is only the 0-thickness penetration value of the Bragg curve (which for light ions is generally well-below the maximum dE/dx). Significant further investigation of the involved molecular dynamics and proto-bubble formation mechanics is required.

Acknowledgments

This work was funded in part by the former Nuclear Physics Center of the University of Lisbon, and by grants IF/00628/2012/CP0171/CT0008, PTDC/FIS/115733/2009 and PTDC/FIS/121130/2010 of the Portuguese Foundation for Science and Technology (FCT). The activities of Felizardo are supported by FCT grant SFRH/BPD/94028/2013. Additional FCT support through projects UID/Multi/04349/2013 and PTDC/EEI-ELC/2468/2014 is gratefully acknowledged, as also the assistance of L.C. Alves in the measurements of the various droplet size distributions.

References

[1] "Superheated Emulsion Detector", adopted by the International Commission on Radiation Units and Measurement (ICRU) and International Organization for Standardization (ISO) to encompass any device using superheated droplets: S.C. Roy, Rad. Phys. and Chem. 61; 2001. p. 271.
[2] E. Behnke, et al., ImprovedSpin-Dependent WIMP Limits from a Bubble Chamber, Science 319 (2008) 933.
[3] M.B. Smith, H.R. Andrews, H. Ing, M.R. Koslowsky, Response of the bubble detector to neutrons of various energies, Radiat. Prot. Dosim. 164 (2015) 203.
[4] F. Aubin, M. Auger, M.-H. Genest, G. Giroux, R. Gornea, R. Faust, C. Leroy, L. Lessard, J.-P. Martin, T. Morlat, et al., Discrimination of nuclear recoils from alpha particles with superheated liquids, New Journ. Phys. 10 (2008) 103017.
[5] M. Felizardo, T. Morlat, A.C. Fernandes, et al., First results of the phase II SIMPLE dark matter search, Phys. Rev. Lett. 105 (2010) 211301.
[6] A.C. Fernandes, J.P. Santos, J.G. Marques, A. Kling, A.R. Ramos, N.P. Barradas, Validation of the monte carlo model supporting core conversion of the portuguese research reactor (RPI) for neutron fluence rate determinations, Ann. Nucl. Energy 37 (2010) 1139.
[7] S. Archambault, F. Aubin, M. Auger, et al., New insights into particle detection with superheated liquids, New Journ. Phys. 13 (2011) 043006.
[8] A.C. Kamaha, Improved Limits on the Existence of Dark Matter: the Final Results from the PICASSO Experiment, (Ph.D. thesis), Queen's University, Canada March (unpublished), 2015.
[9] M. Das, S. Seth, S. Saha, S. Bhattacharya, P. Bhattacharjee, Neutron-gamma discrimination by pulse analysis with superheated drop detector, Nucl. Instrum. Meth. A622 (2010) 196.
[10] P.K. Mondal, S. Seth, M. Das, P. Bhattacharjee, Study of low frequency acoustic signals from superheated droplet detector, Nucl. Instrum. Meth. A729 (2013) 182.
[11] S. Seth, M. Das, Radiation LET and drop size dependence of the low frequency signal from tiny superheated droplets, Nucl. Instrum. Meth. A837 (2016) 92.
[12] F. Seitz, On the theory of the bubble chamber, Phys. Fluids 1 (1958) 2.
[13] (a) L. Rayleigh, On the pressure developed in a liquid During the collapse of a spherical cavity, Philos. Mag. 34 (1917) 94;
(b) M.S. Plesset, The dynamics of cavitation bubbles, ASME J. Appl. Mech. 16 (1949) 228.

[14] M.S. Plesset, S.A. Zwick, The growth of vapor bubbles in superheated liquids, J. Appl. Phys. 25 (1954) 493.
[15] N. Yu, N.S. Martynyuk, Smirnov, sound generation in superheated liquids by heavy charged particles, Sov. Phys. Acoust. 37 (1991) 376.
[16] Y.Y. Sun, B.T. Chu, R.E. Apfel, Radiation-induced cavitation process in a metastable superheated liquid: i. Initial and pre-bubble formation stages, Journ. Comput. Phys. 103 (1992) 116125.
[17] Y.Y. Sun, B.T. Chu, R.E. Apfel, Radiation-induced cavitation process in a metastable superheated liquid: ii. Interface formation and post-interface formation stages, Journ. Comput. Phys. 103 (1992) 126140.
[18] H.Y. Kwak, S.D. Oh, C.H. Park, Bubble dynamics on the evolving bubble formed from the droplet at the superheated limit, Int. Journ. Heat. Mass Transf. 38 (1995) 1709.
[19] L.K. Pan, C.-K.C. Wang, Superheated-liquid-droplet technique for measuring alpha decays in uranium solutions, Nucl. Instrum. Meth. A420 (1999) 345.
[20] M.C. Ghilea, D.D. Meyerhofer, T.C. Sangster, Neutron-induced nucleation inside bubble chambers using Freon 115 as the active medium, Nucl. Instrum. Meth. A648 (2011) 210.
[21] F. d'Errico, Radiation dosimetry and spectrometry with superheated emulsions, Nucl. Instrum. Meth B184 (2001) 229.
[22] L.D. Landau, E.M. Lifschitz, Fluid Mechanics vol VI, Oxford: Butterworth-Heinemann.
[23] M. Das, Searching for universal behaviour in superheated droplet detector with effective recoil nuclei, Pramana 80 (2013) 994.
[24] S.L. Guo, T. Doke, L. Li, et al., Comparison between theoretical model and experimental calibrations and its inference for track formation in bubble detectors, Radiat. Meas. 40 (2005) 239.
[25] M.J. Harper, J.C. Rich, Radiation-induced nucleation in superheated liquid droplet neutron detectors, Nucl. Instrum. Meth. A336 (1993) 220.
[26] F. Poesposoetlipto, E. Hugentobler, A study on bubble formation in the bubble chamber, Helv. Phys. Acta 43 (1970) 203.
[27] M. Das, T. Sawamura, Estimation of Nucleation Parameter for Neutron-induced Nucleation in Superheated Emulsion, Nucl. Instrum. Meth. A531 (2004) 577.
[28] M. Das, T. Sawamura, Superheated emulsions in neutron spectrometry by varying ambient pressure, Nucl. Instrum. Meth. A536 (2005) 123.
[29] S. Seth, M. Das, S. Bhattacharya, P. Bhattacharjee, S. Saha, The nucleation parameter for heavy-ion induced bubble nucleation in superheated emulsion detector, Journ. Instrum. 8 (2013) P05001.
[30] T. Morlat, et al., The role of additives towards increasing the SIMPLE SDD lifetime, Nucl. Instrum. Meth. A560 (2006) 339.
[31] T. Morlat, Amélioration de la Durée de Vie des Détecteurs de Gouttelettes de Fréon en Surchauffe en vue de la Détection de Matière Cachée (PhD thesis), University of Paris 2004, p. 6 (unpublished).
[32] C. Joly-Duhamel, D. Hellio, A. Ajdari, All gelatin networks: 2. The master curve for elasticity, Langmuir 18 (2002) 7158.
[33] T. Boudoua, J. Ohayona, C. Picartb, P. Tracquia, Extension de la Caractérisation des Propriétés Mécaniques d'Échantillons Biologiques par la Technique d'Aspiration par Micropipette: Application aux milieux isotropes, 18 ème Congrès Français de Mécanique Grenoble, 27-31 août, 2007.
[34] M. Felizardo, T.A. Girard, T. Morlat, et al., (The simple collaboration), phase II of the simple dark matter search, Phys. Rev. D89 (2014) 072013.
[35] M. Felizardo, T. Morlat, T.A. Girard, et al., Superheated droplet detector response to fabrication variations, Nucl. Instrum. Meth. A614 (2010) 278.
[36] NIST, REFPROP code, NIST Standard Database 23, V.7, 2002.
[37] C.L. Yaws, M.A. Satyro, Enthalpy of vaporization-organic compounds, in: C. L. Yaws (Ed.), Thermophysical Properties of Chemicals and Hydrocarbons, William Andrew Publishing, Norwich, NY, 2009, pp. 309–400 (Chapter 7).
[38] H.W. Bonin, G.R. Desnoyers, T. Cousins, Fast neutron dosimetry and spectroscopy using bubble detectors, Radiat. Prot. Dosim. 46 (2001) 265.
[39] A.C. Fernandes, A. Kling, M. Felizardo, T.A. Girard, et al., Neutron background signal in superheated droplet detectors of the phase II simple dark matter search, Astro. Phys. 76 (2016) 48.
[40] J. Ziegler, Stopping and Range of Ions in Matter: ⟨http://www.srim.org/⟩.
[41] J. Puibasset, Étude de Suspensions de Gouttelettes de Fréon en Surchauffe en Vue de la Réalisation d'un Détecteur de Matiére Cachée Galactique, PhD thesis, Univ. Paris VII, 2000 (unpublished).
[42] Table of Isotopes: R.B. Firestone, V.S. Shirley, C.M. Baglin; S.Y.F. Chu, J. Zipkin (Eds.), John Wiley & Sons, Inc., , 1976.
[43] P. Denzel, J. Diemand, R. Angélil, Molecular dynamics simulations of bubble nucleation in dark matter detectors, Phys. Rev. E93 (2016) 013301.
[44] J.E. Grindler, The Radiochemistry of Uranium, National Academy of Science-National Research Council, Washington, 1962.
[45] A.L. Mills, D.H. Logsdail, Solvent Extraction and Ion Exchange in the Nuclear Fuel Cycle, Ellis Horwood Limited, London, 1985.
[46] P.A.G. OÕhare, E.H.P. Cordfunke, The Chemical Thermodynamics of Actinide Elements and Compounds, Part3 Miscellaneous Actinide Compounds, International Atomic Energy Agency, Vienna, 1978.
[47] J.E. Popielarczky Jr., Self-diffusion Phenomena in Thallium Amalgams, Ph.D. Thesis, Georgia Institute of Technology, 1975.
[48] M.J. Harper, A. Theoretical, Model of a Superheated Liquid Droplet Neutron Detector, PhD thesis, Univ. Maryland, 1991 (unpublished).
[49] F. d'Errico, R.E. Apfel, G. Curzio, R. Nath, D.T. Bartlett, J. Boehm, H. Hyvoenen, Electronic neutron personal dosimetry with superheated drop detectors, Radiat. Prot. Dosim. 96 (2001) 261.